

## Synthesis of NiO-doped Fe<sub>3</sub>O<sub>4</sub>/chitosan-PVA composites for tetracycline degradation under visible light irradiation

Poedji Loekitowati Hariani<sup>1,2\*</sup> , Addy Rachmat<sup>1,2</sup> , Hermansyah<sup>1</sup> , Elpera Yulianti<sup>1</sup> 

<sup>1</sup> Department of Chemistry, Faculty of Mathematics and Natural Sciences, Universitas Sriwijaya, Jalan Palembang-Prabumulih, Indralaya, Ogan Ilir 30662, Indonesia

<sup>2</sup> Research Group on Magnetic Materials, Department of Chemistry, Faculty of Mathematics and Natural Sciences, Universitas Sriwijaya, Jalan Palembang-Prabumulih, Indralaya, Ogan Ilir 30662, Indonesia

\* Corresponding author's e-mail: [puji\\_lukitowati@mipa.unsri.ac.id](mailto:puji_lukitowati@mipa.unsri.ac.id)

### ABSTRACT

Tetracycline contamination adversely affects aquatic ecosystems and increases the likelihood of antibiotic-resistant bacterium development, posing substantial risks to both environmental and human health. Consequently, there is a pressing need for efficient technologies to break down and eliminate tetracycline from water sources. This study aimed to synthesis a Fe<sub>3</sub>O<sub>4</sub>/Chi-PVA@NiO composite for photocatalytic degradation of tetracycline. Crosslinked chitosan (Chi) and polyvinyl alcohol (PVA) were applied to enhance the mechanical strength and increasing the physical and chemical stability of composites. XRD, UV-DRS, SEM-EDS, VSM, and FTIR were employed for characterization. The composite material exhibits magnetic characteristic, evidenced by a saturation magnetization of 67.13 emu/g and a band gap measuring 1.86 eV. The magnetic characteristics enhance the separation efficiency of the composite following the photocatalytic process with an external magnet and low band gap values, which enable degradation to occur under visible light radiation. The maximum degradation efficiency was attained at a pH of 5, a tetracycline concentration of 20 mg/L, a composite dosage of 0.5 g/L, and an irradiation time of 100 min with a degradation efficiency of 98.20%. The rate of degradation kinetics approximates a pseudo-first-order model in which the value of the degradation constant decreases as the concentration of tetracycline increases. The catalyst exhibited outstanding stability and reusability, achieving a high degradation efficiency of 94.10% over five consecutive cycles. The FTIR analysis revealed no notable alterations in the functional groups of the composite both prior and following the photocatalytic degradation process. This research offers an efficient and eco-friendly approach for removing tetracycline contaminants from the environment.

**Keywords:** antibiotic removal, degradation, Fe<sub>3</sub>O<sub>4</sub>/Chi-PVA@NiO, environmental remediation.

### INTRODUCTION

Tetracycline belongs to a class of wide-spectrum antibiotics characterized by a phenanthrene parent nucleus and is commonly used in both human healthcare and animal husbandry [Zhao et al., 2019; Sharma et al., 2022]. Approximately 75% of the absolute quantity of tetracycline consumed by the body is eliminated through feces and urine in the form of its original molecular structure [Li et al., 2020]. Tetracycline exhibits hydrophilicity, biological activity, high stability, a slow degradation rate, and is extremely hazardous to aquatic creatures that are not its intended target [Liu et al., 2019; Cycon et

al., 2019]. The accumulation of antibiotic residues in water sources fosters antibiotic resistance genes, resulting in bacteria that are immune to antibiotics in aquatic ecosystems [Wei et al., 2023; Wang et al., 2020]. The deposition of antibiotics via the food chain in the environment can present a significant hazard to humans and ecosystems, leading to an ecological imbalance [Sharma et al., 2022]. Hence, it is crucial to eliminate tetracycline from wastewater, employing a pragmatic, cost-effective approach that avoids the generation of secondary contaminants. Diverse methodologies have been utilized to eradicate tetracycline from wastewater, including coagulation-flotation [Saitoh et al.,

2017], osmosis membrane [Guo et al., 2020], ozonation [Wang et al., 2020], biodegradation [Yan et al., 2022], adsorption [Ersan and Dogan, 2023], and photocatalytic degradation [Harikumar et al., 2024]. advanced oxidation processes (AOPs), particularly photocatalytic oxidation techniques, represent effective approaches for the elimination of tetracycline from wastewater. This approach demonstrates efficacy in eliminating antibiotics, consume minimal energy, and is environmentally sustainable [Chen et al., 2020; Huang et al., 2023]. Nonetheless, traditional photocatalysts encounter challenges, such as broadband gaps and elevated electron recombination rates, which considerably hinder degradation efficiency [Long et al., 2020]. NiO is categorized as a p-type semiconductor with promising applications as a photocatalyst. NiO exhibits chemical and thermal stability, outstanding conductance properties, and is non-toxic [Fatimah et al., 2024]. NiO exhibits a significant band gap ranging from 3.0 to 4.0 eV, which restricts its absorption to ultraviolet light, accounting for merely about 3% of solar energy. Additionally, NiO tends to experience rapid recombination, meaning that electrons and holes do not remain separated long enough to perform the desired reactions on the catalyst surface, resulting in lower degradation efficiency [Han et al., 2024; Hariani et al., 2023]. Therefore, improving photocatalysts to increase their efficiency is a significant area of research. Various modifications of NiO have been reported, including NiO/Fe<sub>2</sub>O<sub>3</sub> [Han et al., 2024], NiFe<sub>2</sub>O<sub>4</sub>@NiO [Tripta and Rana, 2024], and NiO/ZnO/g-C<sub>3</sub>N<sub>4</sub> [Jayaprakash et al., 2024]. Modifying ferrite compounds can decrease the band gap and improve photocatalytic efficiency. Fe<sub>3</sub>O<sub>4</sub> is a ferrite compound with unique properties, including superparamagnetism, biodegradability, and low toxicity. Furthermore, Fe<sub>3</sub>O<sub>4</sub> exhibits a modest band gap of 1.2 eV, is straightforward to synthesize, and its magnetic characteristics can aid in separating catalysts following the photocatalytic degradation process [Cui et al., 2022].

A plethora of studies have focused on the utilization of organic materials to augment the efficiency of photocatalytic degradation by enhancing catalyst stability, reducing aggregation and dissolving effects, therefore facilitating the immobilization of the catalyst on a template. Chitosan (Chi) is a biopolymer obtained through the deacetylation of chitin. It exhibits excellent biocompatibility, biodegradability, non-toxicity, and antimicrobial properties [Adeli et al., 2019; Sanchez-Machoda et al., 2024]. However, chitosan exhibits limited

mechanical properties and a tendency to dissolve readily in acidic environments [Luk et al., 2014]. Polyvinyl alcohol (PVA) is a hydrophilic polymer, exhibiting low toxicity and good mechanical strength [Kamoun et al., 2017; Mohamadkhani et al., 2024]. PVA serves as a crosslinker that improves the stability of chitosan through the generation of hydrogen bonds with the amino groups present in chitosan molecules [Habiba et al., 2019; Sopianrao and Sreedhar, 2024].

This study focuses on the synthesis of Fe<sub>3</sub>O<sub>4</sub>/Chi-PVA@NiO composites, which will be used in tetracycline photocatalysis. Fe<sub>3</sub>O<sub>4</sub> acts as the core, while chitosan-PVA forms the shell, with NiO dispersed throughout the chitosan-PVA matrix through cross-linking. By doped NiO with Fe<sub>3</sub>O<sub>4</sub> and chitosan-PVA, the photocatalytic ability can be increased, so that the degradation process becomes more efficient. The magnetic properties of the catalyst make it easier to separate the catalyst from the waste using a magnet. Additionally, the study explores the photocatalytic degradation kinetic and the reusability of the catalyst. This research aims to deliver an efficient, sustainable solution for the breakdown of tetracycline and analogous organic contaminants, thereby advancing eco-friendly solutions for water treatment.

## MATERIALS AND METHODS

### Materials

The utilized chemicals comprise FeCl<sub>2</sub>·4H<sub>2</sub>O, FeCl<sub>3</sub>·6H<sub>2</sub>O, NaOH, HCl, polyvinyl alcohol (PVA), CH<sub>3</sub>COOH, NiCl<sub>2</sub>, NaCl, and tetracycline sourced from Merck, Germany. Chitosan is sourced from Natura Chem Abadi in Indonesia, exhibiting a Degree of Deacetylation greater than 99.5%.

### Synthesis of Fe<sub>3</sub>O<sub>4</sub>

The synthesis of Fe<sub>3</sub>O<sub>4</sub> followed the procedure of Hariani et al. [2023]. 1.988 g of FeCl<sub>2</sub>·4H<sub>2</sub>O and 5.406 g of FeCl<sub>3</sub>·6H<sub>2</sub>O were added to 10 mL of distilled water at room temperature, maintaining a molar ratio of 2:1. A 2 M NaOH solution was incrementally introduced to the mixture while being stirred gently with a magnetic stirrer at 250 rpm, under a flow of N<sub>2</sub> gas at 40 °C. The process is conducted until the pH attains 10. The black residue was washed numerous times with distilled water to get a neutral pH, then dried at 70 °C for 3 hours in an oven.

### Synthesis of Fe<sub>3</sub>O<sub>4</sub>/Chi-PVA

The synthesis of Fe<sub>3</sub>O<sub>4</sub>/Chi-PVA followed the procedure for synthesizing Fe<sub>3</sub>O<sub>4</sub>. The mixture was incorporated into the chitosan while being stirred at 150 rpm with a shaker until a homogeneous consistency was achieved, which took approximately 60 min. A 2 M NaOH solution was incrementally added while the solution was being stirred with a magnetic stirrer at 250 rpm under a flow of N<sub>2</sub> gas at a temperature of 40 °C until the pH reached approximately 10. During stirring, 80 mL of a 2% PVA solution was added to the Fe<sub>3</sub>O<sub>4</sub>/Chi mixture and mixed for 60 min using a shaker. The Fe<sub>3</sub>O<sub>4</sub>/Chi-PVA precipitate was then rinsed with distilled water till achieving a neutral pH, followed by drying in an oven at 70 °C for 3 hours.

### Synthesis of Fe<sub>3</sub>O<sub>4</sub>/Chi-PVA@NiO

The synthesis of Fe<sub>3</sub>O<sub>4</sub>/Chi-PVA@NiO followed the procedure for synthesizing Fe<sub>3</sub>O<sub>4</sub>/Chi-PVA but was followed by the addition of 0.48 g of NiCl<sub>2</sub> and a modification based on the method by Vijeth et al. [2020]. The mixture was sonicated for 1 hour to achieve a uniform dispersion. The entire mixture was subsequently placed into a Teflon-stainless steel autoclave and subjected to heating at 190 °C for 7 hours. The suspension was filtered, rinsed with distilled water and ethanol, and then dried at 60 °C for 3 hours. The Fe<sub>3</sub>O<sub>4</sub>/Chi-PVA@NiO composite was calcined at 400 °C for a duration of 2 hours.

### Material characterization

The synthesized material was characterized using X-ray diffraction (XRD PANalytical) with incident radiation of Cu K $\alpha$  ( $\lambda = 1.5405$ ) and a range of  $2\theta = 10$ – $90^\circ$  to ascertain the crystal phase and the purity of the photocatalyst. The morphology was examined utilizing a Scanning Electron Microscope integrated with an energy dispersive spectrometer (SEM-EDS Thermo Fisher Scientific). The band gap was determined using UV–visible diffuse reflectance spectroscopy (UV Vis DRS Cary 60). The magnetic properties of the composite photocatalyst were assessed utilizing a vibrating sample magnetometer (VSM Oxford Type 1.2 T). The functional groups of the composite were analyzed using a Fourier transform infrared spectrometer (FT-IR Nicolet iS5 Thermo Scientific) with KBr pellets with range of 400–4000 cm<sup>-1</sup>.

### pHpzc of Fe<sub>3</sub>O<sub>4</sub>/Chi-PVA@NiO

The pHpzc was established by utilizing 100 mL of a 0.01 N NaCl solution, with the pH modified through the incorporation of 0.1 N HCl and NaOH to achieve a pH range of 2–12. Additionally, 0.1 g of the Fe<sub>3</sub>O<sub>4</sub>/Chi-PVA@NiO composite was incorporated into each flask. The solution stirred for 24 h at a rotational speed of 300 rpm. The pHpzc was determined from the  $\Delta$ pH versus pHi plot when the initial pH minus final pH equals 0 [Golrizkhatami et al., 2023; Islam et al., 2024].

### Experimental investigation of photocatalytic breakdown of tetracycline

Photocatalytic degradation was evaluated using 100 mL of tetracycline solution and a catalyst dose of 0.25 g/L. Photocatalytic variables include the pH of the tetracycline solution (3–9), the concentration of the tetracycline solution (20–80 mg/L) and the dose of the Fe<sub>3</sub>O<sub>4</sub>/Chi-PVA@NiO composite (0.25–1.0 g/L). The sample was then placed in a reactor with constant stirring (200 rpm, 25 °C) for 40 min to reach adsorption equilibrium. After that, irradiation was carried out with 20-min intervals under constant stirring for 120 min. The radiation source used was a visible lamp (xenon lamp 300 W,  $\lambda = 385$ – $740$  nm) placed 15 cm from the sample. The absorbance of solution after photocatalysis was measured using a UV-Vis spectrophotometer.

## RESULTS AND DISCUSSION

### Characterization of Fe<sub>3</sub>O<sub>4</sub>/Chi-PVA@NiO composite

The analysis of crystallinity and phase structure of Fe<sub>3</sub>O<sub>4</sub>, Fe<sub>3</sub>O<sub>4</sub>/Chi-PVA and Fe<sub>3</sub>O<sub>4</sub>/Chi-PVA@NiO composite are presented in Figure 1. The  $2\theta$  diffraction observed at angles of  $30.26^\circ$ ,  $35.49^\circ$ ,  $43.37^\circ$ ,  $53.57^\circ$ ,  $57.02^\circ$ , and  $62.89^\circ$  aligns with the hkl planes (220), (311), (222), (400), (422), (511), and (440), which are associated with the spinel phase of Fe<sub>3</sub>O<sub>4</sub> (JCPDS No. 065-0731). The diffraction peaks of Fe<sub>3</sub>O<sub>4</sub> modified with chitosan and PVA remained unchanged. The amorphous characteristics of chitosan-PVA result solely in a reduction of intensity (Figure 1b). This suggests that the structure of Fe<sub>3</sub>O<sub>4</sub> remains unchanged. Peaks observed at  $2\theta = 37.28^\circ$ ,  $43.29^\circ$ ,  $62.92^\circ$ , and  $75.61^\circ$  confirm the presence of NiO

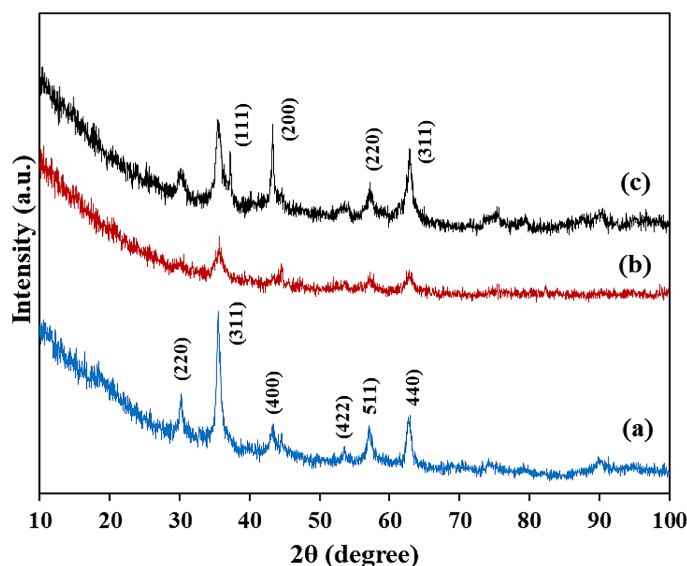


**Figure 1.** XRD patterns of (a)  $\text{Fe}_3\text{O}_4$ , (b)  $\text{Fe}_3\text{O}_4/\text{Chi-PVA}$ , and (c)  $\text{Fe}_3\text{O}_4/\text{Chi-PVA@NiO}$  composites

in  $\text{Fe}_3\text{O}_4/\text{Chi-PVA}$ , corresponding to tetragonal phases based on the crystal planes (111), (200), (220), and (311) as per JCPDS No. 04-0835. Figure 1c shows that the XRD pattern revealed the existence of two material phases, specifically  $\text{Fe}_3\text{O}_4$  and NiO, confirming the proper synthesis of  $\text{Fe}_3\text{O}_4/\text{Chi-PVA/NiO}$  composites. The peaks of  $\text{Fe}_3\text{O}_4$  and NiO exhibit overlapping characteristics, resulting in broader peaks, with increased intensity observed at  $2\theta$  approximately  $43^\circ$  and  $62^\circ$ . The crystallite sizes of  $\text{Fe}_3\text{O}_4$  and NiO, calculated using the Scherrer formula, are 16.5 nm and 21.2 nm, respectively. The crystallite size of  $\text{Fe}_3\text{O}_4$  obtained in this study is significantly smaller than other studies employing similar coprecipitation methods, which reported a crystallite size of 122.66 nm [Said et al., 2022]. In contrast, the crystallite size of NiO is consistent with the findings of other researchers, measuring around 21 nm [Tripta and Rana, 2023].

The SEM images of  $\text{Fe}_3\text{O}_4$  exhibit greater homogeneity than the  $\text{Fe}_3\text{O}_4/\text{Chi-PVA}$  and  $\text{Fe}_3\text{O}_4/\text{Chi-PVA@NiO}$  composites. The findings align with numerous other studies that describe the morphological characteristics of  $\text{Fe}_3\text{O}_4$ , specifically its spherical shape and tendency to agglomerate with varying diameters [Vishwakarma et al., 2023]. The application of chitosan and PVA results in larger particle sizes that exhibit variability in their dimensions. The morphology of the  $\text{Fe}_3\text{O}_4/\text{Chi-PVA@NiO}$  composite resembles that of  $\text{Fe}_3\text{O}_4/\text{Chi-PVA}$ , yet it exhibits a larger particle size and features interstitial space (Figure 2). The elemental composition from the EDS

analysis of  $\text{Fe}_3\text{O}_4/\text{Chi-PVA@NiO}$  is presented in Table 1. The detection of C and N elements is attributed to chitosan, while the presence of Ni suggests that NiO has been distributed on the surface of  $\text{Fe}_3\text{O}_4/\text{Chi-PVA}$ .

Figures 3a and 3b present the UV–vis DRS spectra along with the band gap assessment of the  $\text{Fe}_3\text{O}_4$ ,  $\text{Fe}_3\text{O}_4/\text{Chi-PVA}$ , and  $\text{Fe}_3\text{O}_4/\text{Chi-PVA@NiO}$  composites. The absorbance was recorded within range of 200 to 900 nm. Notable absorption band for all three was observed in the 300–400 nm range. However, in  $\text{Fe}_3\text{O}_4$ , a peak appears at 620 nm. Kouotou et al. [2018] found that  $\text{Fe}_3\text{O}_4$  absorption at 650 nm which was within the visible region. The absorption of NiO typically takes place in the range of 330–380 nm, associated with the d-d transition of  $\text{Ni}^{2+}$  ions within its crystal structure [Hariani et al., 2023]. This absorption band is associated with electron transitions from the valence band to the conduction band, signifying its semiconducting properties. The maximum absorbance of  $\text{Fe}_3\text{O}_4/\text{Chi-PVA@NiO}$  was recorded at 380 nm. The value of the band gap ( $E_g$ ) was calculated using the equation below:

$$(\alpha h\nu)^n = A(h\nu - E_g) \quad (1)$$

The coefficient of optical absorption is represented by  $\alpha$ , while  $h\nu$  denotes the photon energy. For the NiO semiconductor material, the value of  $n$  has been established as 2, signifying an indirect band gap, while  $A$  represents a constant. The band gap values of  $\text{Fe}_3\text{O}_4$ ,  $\text{Fe}_3\text{O}_4/\text{Chi-PVA}$ , and  $\text{Fe}_3\text{O}_4/\text{Chi-PVA@NiO}$  composites are less than 2.0 eV. There is an observed increase in

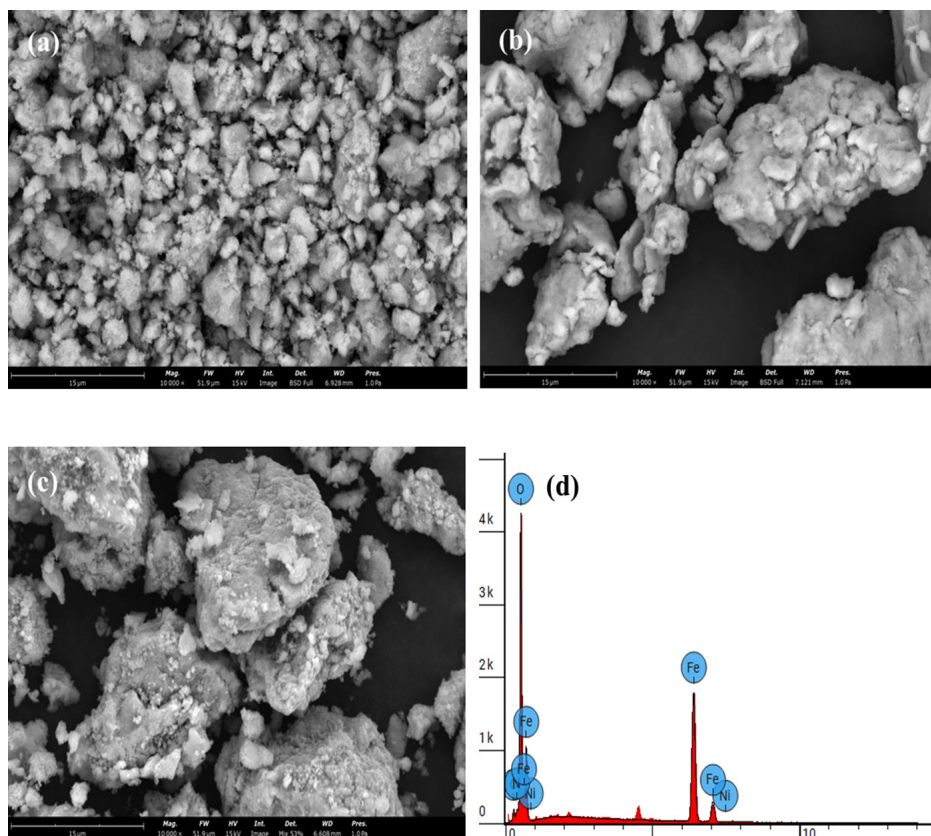


Figure 2. Morphology as observed with SEM of (a) Fe<sub>3</sub>O<sub>4</sub>, (b) Fe<sub>3</sub>O<sub>4</sub>/Chi-PVA, (c) Fe<sub>3</sub>O<sub>4</sub>/Chi-PVA@NiO composites, and (d) EDS spectra of Fe<sub>3</sub>O<sub>4</sub>/Chi-PVA@NiO composites

Table 1. Elemental composition of Fe<sub>3</sub>O<sub>4</sub>/Chi-PVA@NiO composite

Element	Atomic conc. (%)	Weight conc. (%)
Fe	25.21	54.22
O	52.22	31.31
C	14.79	6.42
N	5.57	3.02
Ni	2.21	5.03

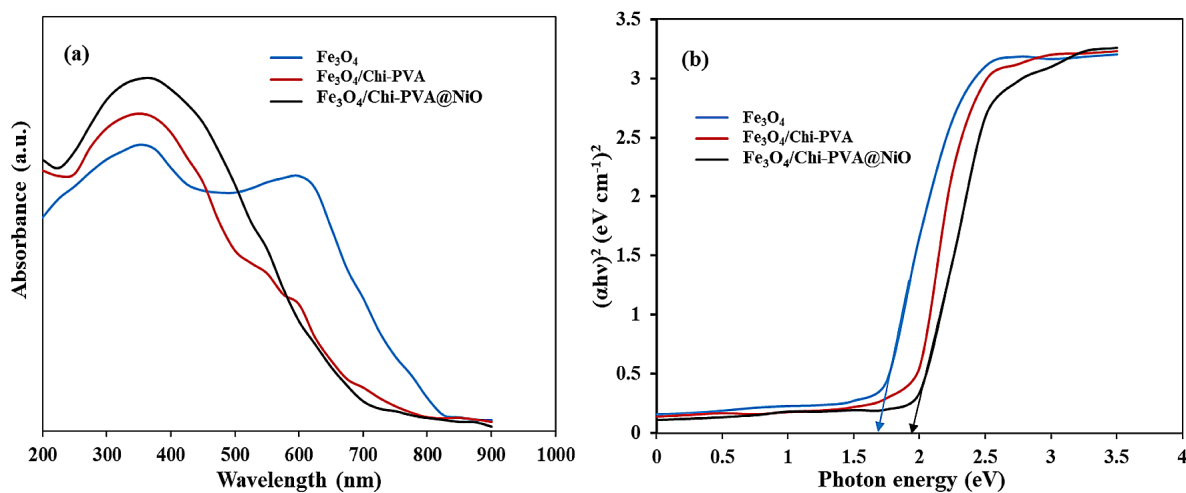


Figure 3. (a) UV-DRS absorbance spectra and (b) Tauc's plot of Fe<sub>3</sub>O<sub>4</sub>, Fe<sub>3</sub>O<sub>4</sub>/Chi-PVA and Fe<sub>3</sub>O<sub>4</sub>/Chi-PVA@NiO composites

the band gap value of  $\text{Fe}_3\text{O}_4$ , with values of 1.62, 1.78, and 1.86 eV for  $\text{Fe}_3\text{O}_4$ ,  $\text{Fe}_3\text{O}_4/\text{Chi-PVA}$ , and  $\text{Fe}_3\text{O}_4/\text{Chi-PVA}@\text{NiO}$ , respectively. The observed increase is attributed to the incorporation of NiO, which possesses a band gap value of approximately 3.5 eV. The magnetic properties of  $\text{Fe}_3\text{O}_4$  and each composite were analyzed by applying an external magnetic field ( $-15$  kOe and  $+15$  kOe) presented in Figure 4. The graph of magnetization vs applied magnetic field properly demonstrates the ferromagnetic characteristics. The saturation magnetization ( $M_s$ ) value of  $\text{Fe}_3\text{O}_4$  is measured at 81.06 emu/g, while the incorporation of chitosan-PVA, a non-magnetic substance, results in a decreased to value of 70.59 emu/g. The composite of  $\text{Fe}_3\text{O}_4/\text{Chi-PVA}@\text{NiO}$  exhibits a  $M_s$  value of 67.13 emu/g. The magnetic properties observed in this study surpass those reported in previous research, specifically showing  $\text{Fe}_3\text{O}_4$  at 55.3 emu/g, which decreases to 30.4 emu/g when formed into a  $\text{Fe}_3\text{O}_4/\text{TiO}_2$  composite [Tumbelaka et al., 2022].

## PHOTOCATALYTIC STUDIES

### Effect of pH, initial concentration of tetracycline, and catalyst dosage

Photocatalytic degradation activity of the synthesized composite was evaluated against tetracycline. The experiment was conducted without light for 40 min, followed by the procedure with visible light. The ratio of tetracycline

concentration at each time ( $C_t$ ) after photocatalytic degradation and the initial concentration of tetracycline ( $C_0$ ) was determined. The pHPzc of the  $\text{Fe}_3\text{O}_4/\text{Chi-PVA}@\text{NiO}$  composite was determined to be 6.4 (Figure 5a). pHPzc denotes the pH level at which a material's surface exhibits a neutral charge. The data presented in Figure 5b indicates that the optimum pH for photocatalytic activity is at pH 5. Tetracycline exhibits three pKa values: 3.3, 7.7, and 9.7 [Marzbali et al., 2016]. The protonation or deprotonation reveals four distinct ionic species at varying pH levels: cationic ( $\text{TC}^+$ ), zwitterionic ( $\text{TC}^\pm$ ), anionic ( $\text{TC}^-$ ), and dianion ( $\text{TC}^{2-}$ ) [Zhao et al., 2020; Qin et al., 2022]. At a highly acidic pH ( $\text{pH} < 3.3$ ), tetracycline carries a positive charge, and the surface of the  $\text{Fe}_3\text{O}_4/\text{Chi-PVA}@\text{NiO}$  composite is similarly positively charged, leading to electrostatic repulsion. As pH rises, the tetracycline charge shifts to negative, enhancing the attraction due to the positively charged composite surface ( $< \text{pHPzc}$ ). Comparable findings were observed in the degradation of tetracycline utilizing  $\text{Cr}_2\text{O}_3/\text{ZrO}_2$  nanocomposite [Wei et al., 2023]. Under basic conditions, repulsion occurs between the anionic tetracycline and the negatively charged composite surface, reducing the degraded tetracycline. A different investigation revealed that at a pH of 10, the UV absorption characteristics of tetracycline underwent a shift. The observed phenomenon could be attributed to the elevated levels of  $\text{Na}^+$  in the solution, which could lead to a variation in peak absorption [Zhang et al., 2023]. The concentration effect was examined

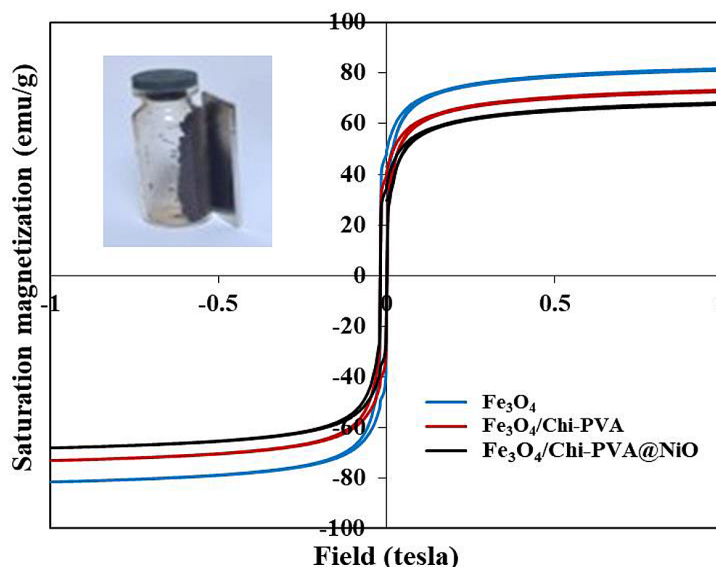


Figure 4. Magnetization curves of  $\text{Fe}_3\text{O}_4$ ,  $\text{Fe}_3\text{O}_4/\text{Chi-PVA}$ , and  $\text{Fe}_3\text{O}_4/\text{Chi-PVA}@\text{NiO}$  composites

with tetracycline concentrations of 20, 40, 60, and 80 mg/L, maintaining a solution pH of 5 and a catalyst dose of 0.25 g/L, as illustrated in Figure 5c. The maximum degradation observed at an initial tetracycline concentration of 20 mg/L reached 92.89%. Raising the initial tetracycline concentrations to 40, 60, and 80 mg/L resulted in degradation efficiencies of 89.0%, 83.70%, and 78.90%, respectively. The composite surface is restricted in its availability, which can be exacerbated by increased concentration, resulting in tetracycline competition [Zhang et al., 2023]. Elevating the tetracycline concentration will additionally obstruct the light source radiation from reaching the catalyst [Hariani et al., 2022].

Figure 5d depicts the breakdown rate of tetracycline relative to the catalyst dosage. The degradation efficiency improved from 92.89% at a dose of 0.25 g/L to 98.20% at a dose of 0.5 g/L for 100 min. An increase in the catalyst dose is associated with a rise in the number of active sites on the catalyst surface for interaction with tetracycline.

However, the degradation efficiency declined at a concentration of 0.75 g/L. The catalyst material is an insoluble substance, and its elevated concentration leads to enhanced light scattering. An excessive dosage will lead to increased light scattering, diminish the light transmittance of the solution, and hinder any further enhancement in photocatalyst performance [Yuan et al., 2022].

### Kinetics of photocatalytic degradations

Multiple studies demonstrate that tetracycline degradation follows pseudo-first-order kinetics, as defined by the Langmuir-Hinshelwood model [Han et al., 2024; Golrizkhatami et al., 2023]. The degradation kinetics were examined with tetracycline concentrations varying from 20 mg/L to 80 mg/L, with increments of 20 mg/L, at a constant pH of 5 and a catalyst dose of 0.5 g/L administered. The equation representing the pseudo-first-order process is expressed as follows:

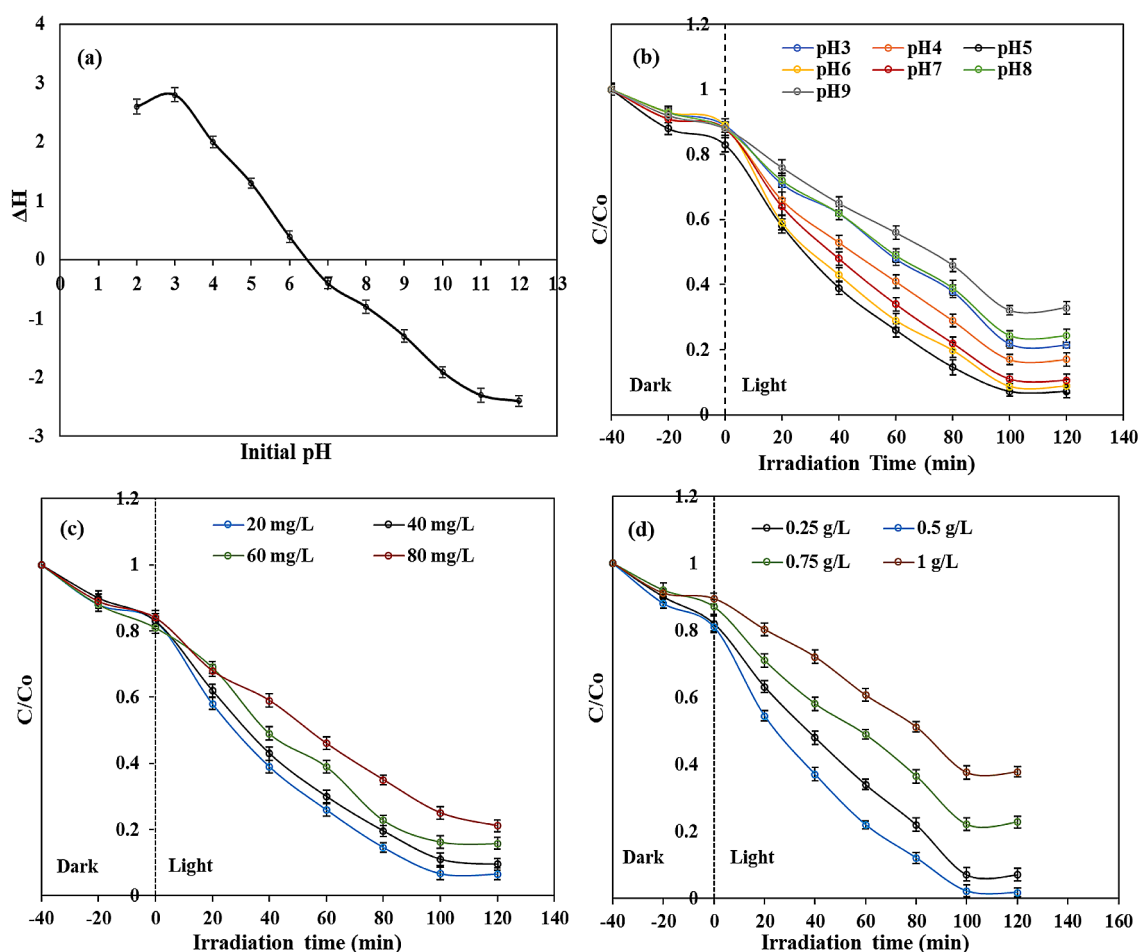
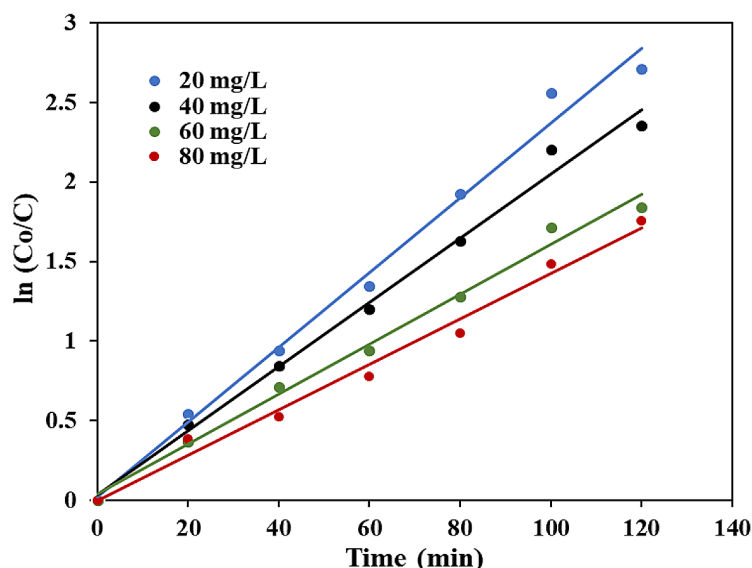


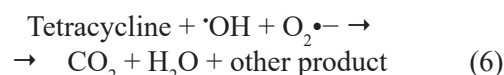
Figure 5. (a)  $pH_{pzc}$  and the effect of (b) pH solution, (c) initial concentration of tetracycline, and (d) catalyst dosage on the degradation of tetracycline



**Figure 6.** Pseudo-first-order kinetic profiles at varying starting doses of tetracycline

$$\ln \frac{C_0}{C} = k_{app} t \quad (2)$$

The curve depicting the correlation between  $\ln C_0/C$  and time ( $t$ ) are illustrated in Figure 6, with  $C_0$  representing the initial concentration of the solution and  $C$  denoting the concentration remaining at any given time. The coefficient of determination ( $R^2$ ) value approaches 1, suggesting a robust relationship between the two variables. The  $k_{app}$  value shows an upward decreasing trend with increased concentration, specifically  $0.0235 \text{ min}^{-1}$ ,  $0.0202 \text{ min}^{-1}$ ,  $0.0157 \text{ min}^{-1}$  and  $0.0143 \text{ min}^{-1}$ . The  $k_{app}$  value is influenced by the concentration of the degraded substance and the catalyst dosage [Sharma et al., 2022; Han et al., 2024]. Understanding the degradation mechanism is important for the development of novel photocatalysts with enhanced efficacy. Exposure of the catalyst with sufficient energy can promote electron excitation from the valence band to the conduction band, so generating holes in the valence band. The interaction of conduction band electrons with dissolved oxygen on the catalyst surface can lead to the formation of superoxide radicals. Within the valence band, holes can undergo the oxidation of water molecules or hydroxyl ions existing on the surface, resulting in the generation of hydroxyl radicals. The mechanism of photocatalytic degradation may be described by the following [Shaban et al., 2020; Hariani et al., 2022].



### Reusability of catalyst

The examination of catalyst stability and utilization is crucial when considering economic implications. The catalytic capacity of the composite was assessed through repetitive tetracycline degradation performed over five consecutive cycles. The catalyst was isolated from the solution after photocatalytic degradation with magnet, then washed, dried, and re-used for another process [Guan et al., 2024]. Figure 7 illustrates the degradation efficiency observed after five consecutive cycles, which were observed at 97.60%, 96.35%, 95.20%, 94.82%, and 94.10%. The decline in catalytic efficiency was posited to be associated with the blockage of active sites, particularly due to the accumulation of residual tetracycline on the surface of catalyst and the leaching of specific Ni ions from the catalyst. The findings of this study surpass the degradation of tetracycline utilizing 2-D  $\text{gC}_3\text{N}_4$  supported  $\text{CoFe}_2\text{O}_4$ , with the catalytic efficiency of the catalyst declining to approximately 86% in the sixth cycle [Gogoi et al., 2023]. It demonstrates that the catalyst exhibits remarkable catalytic stability, leading to substantial cost savings.

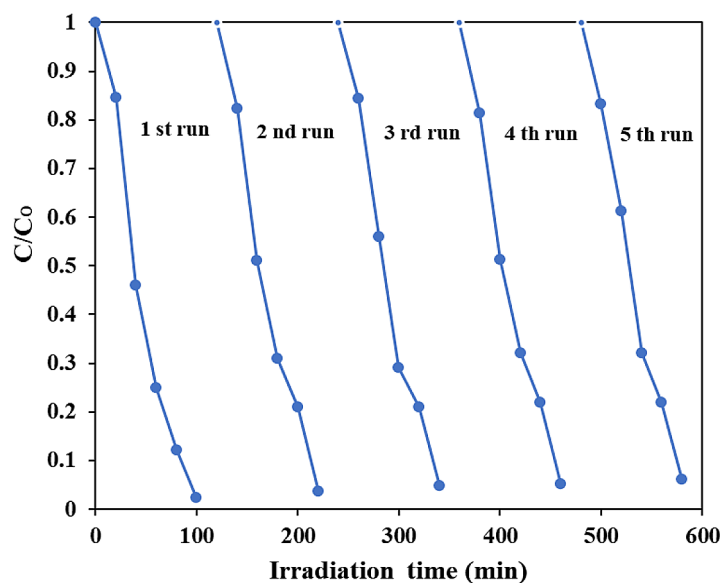


Figure 7. The degrading efficacy of the Fe<sub>3</sub>O<sub>4</sub>/Chi-PVA@NiO composite following five cycles

### FTIR characterization prior and following photocatalytic degradation

FTIR spectra of the Fe<sub>3</sub>O<sub>4</sub>/Chitosan-PVA composite before to and following photocatalysis is depicted in Figure 8. The vibrations of O–H and N–H bonds were detected at 3387 cm<sup>-1</sup>. The bond vibrations of C–H and -CH<sub>2</sub> appeared at 2931 cm<sup>-1</sup> and 1408 cm<sup>-1</sup> which originated from chitosan and PVA. Additionally, the subtle peak observed at 1328 cm<sup>-1</sup> indicates the chitosan amide band [Sanchez-Machoda et al., 2023]. The wave number at 1606 cm<sup>-1</sup> linked to the stretching vibration of the aromatic ring

C–C, while wave number at 1017 cm<sup>-1</sup> is correspond to the C–O–C bond. Metal–oxygen bonds typically appear within the 400–600 cm<sup>-1</sup> wave range. The band near 500 cm<sup>-1</sup> is linked to the overlapping of O–Fe–O bond with Ni–O bond [Ayed et al., 2023; Qin et al., 2024]. The peak was noted at wave numbers 549 and 555 cm<sup>-1</sup> before and following photocatalytic degradation. Both spectra exhibited no shift in wave numbers; only variations in intensity were observed. This behavior indicates that the Fe<sub>3</sub>O<sub>4</sub>/Chitosan-PVA@NiO composite demonstrates remarkable stability. Table 2 presents various catalysts employed in the photocatalytic

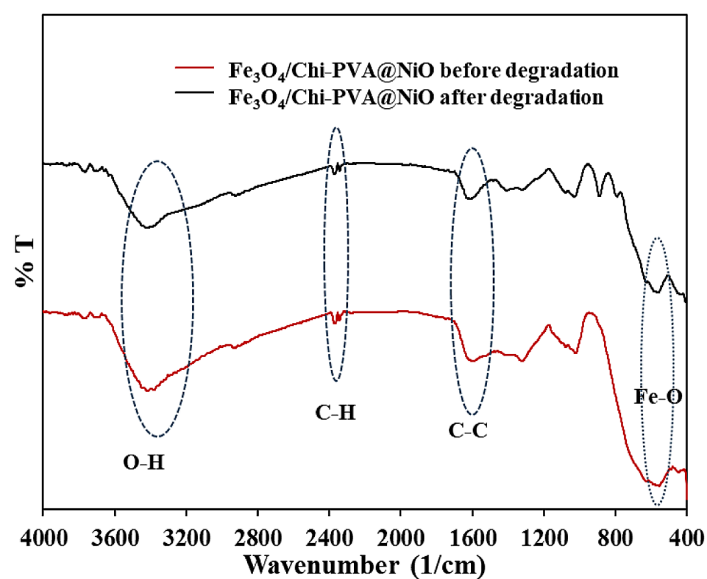


Figure 8. FTIR spectra of Fe<sub>3</sub>O<sub>4</sub>/Chi-PVA@NiO before and after photocatalytic degradation

**Table 2.** Evaluation of tetracycline degradation efficacy utilizing various catalysts.

Photocatalyst	Irrad. time (min)	pH	Concentration (mg/L)	Dosage (g/L)	Degradation (%)	References
Fe <sub>0.25</sub> Cu <sub>0.75</sub> (BDC)@DE/H <sub>2</sub> O <sub>2</sub>	120	3	20	0.5	93	Cui et al. [2022]
Cu <sub>2</sub> O/BiOCl S-scheme	80	4	20	0	90.3	Yuan et al. [2022]
(Bi)BiOBr/rGO	140	–	20	1	98	Jiang et al. [2022]
CuO/Fe <sub>3</sub> O <sub>4</sub> /GO	150	7	30	0.2	97.3	Zhu et al. 2022
Bi <sub>2</sub> WO <sub>6</sub>	180	–	20	0.3	79.68	Chen et al. [2023]
Cr <sub>2</sub> O <sub>3</sub> /ZrO <sub>2</sub>	120	–	50	1	97.1	Wei et al. [2023]
CuS/CdS	50	–	20	0.5	90	Siddhardhan et al. [2023]
BiVO <sub>4</sub> (110)-Fe <sub>2</sub> O <sub>3</sub>	60	–	15	0.4	91.5	Fu et al. [2023]
BiVO <sub>4</sub> /COF	90	–	20	0.2	91.56	Li et al. [2024]
Fe <sub>3</sub> O <sub>4</sub> /Chi-PVA@NiO	100	5	20	0.5	98.20	In this work

degradation of tetracycline as reported in multiple studies. The catalyst from the Fe<sub>3</sub>O<sub>4</sub>/Chi-PVA@NiO composite exhibits superior catalytic efficacy compared to the others.

## CONCLUSIONS

This research demonstrates the successful synthesis of Fe<sub>3</sub>O<sub>4</sub>/Chi-PVA@NiO composite for the photocatalytic degradation of tetracycline. Typically, NiO has a band gap value exceeding 3.0 eV. Modification of NiO with Fe<sub>3</sub>O<sub>4</sub>/Chi-PVA reduces its band gap to below 2 eV, enabling effective use in the visible light spectrum. The composite showed outstanding photocatalytic performance compared to other catalysts, achieving a degradation efficiency of 98.20% at pH 5, tetracycline concentration of 20 mg/L, composite dose of 0.5 g/L, and irradiation for 100 min under visible light. The composite exhibits superior stability, evidenced by its 94.10% degradation ability sustained after five cycles. The result is supported by the FTIR spectra, which reveal no substantial alteration in functional groups before and after photocatalytic degradation. The results of this investigation can offer insightful information, particularly for wastewater treatment applications in environmental remediation.

## Acknowledgments

The author extends gratitude to Direktorat Riset, Teknologi, dan Pengabdian Masyarakat, Direktorat Jenderal Pendidikan Tinggi, Riset, dan Teknologi, Indonesia, for funding the research in compliance with “Kontrak Pelaksanaan Program

Bantuan Operasional Perguruan Tinggi Negeri” under “Penelitian Fundamental” scheme with contract number of 090/E5/PG.02.00.PL/2024.

## REFERENCES

- Adeli H., Khorasani M.T., Parvazinia M. 2019. Wound dressing based on electrospun PVA/chitosan/starch nanofibrous mats: Fabrication, antibacterial and cytocompatibility evaluation and in vitro healing assay. *International Journal of Biological Macromolecules*, 122, 238–254. <https://doi.org/10.1016/j.ijbiomac.2018.10.115>
- Ayed S.B., Mansour L., Vaiano V., Harrath A.H., Ayari F., Rizzo L. 2023. Magnetic Fe<sub>3</sub>O<sub>4</sub>-natural iron ore/calcium alginate beads as heterogeneous catalyst for Novacron blue dye degradation in water by (photo) Fenton process. *Journal of Photochemistry & Photobiology, A: Chemistry*, 438, 1–12. <https://doi.org/10.1016/j.jphotochem.2023.114566>
- Chen D., Cheng Y., Zhou N., Chen P., Wang Y., Li K., Huo S., Cheng P., Peng P., Zhang R., Wang L., Liu H., Liu Y., Ruan R. 2020. Photocatalytic degradation of organic pollutants using TiO<sub>2</sub>-based photocatalysts: A review. *Journal of Cleaner Production*, 268, 1–14. <https://doi.org/10.1016/j.jclepro.2020.121725>
- Chen L., Xu B., Jin M., Chen L., Yi G., Xing B., Zhang Y., Wu Y., Li Z. 2023. Excellent photocatalysis of Bi<sub>2</sub>WO<sub>6</sub> structured with oxygen vacancies in degradation of tetracycline. *Journal of Molecular Structure*, 1278, 1–10. <https://doi.org/10.1016/j.molstruc.2023.134911>
- Cui K., Yang T., Chen Y., Weerasooriya R., Li, G., Zhou K., Chen X. 2022. Magnetic recyclable heterogeneous catalyst Fe<sub>3</sub>O<sub>4</sub>/g-C<sub>3</sub>N<sub>4</sub> for tetracycline hydrochloride degradation via photo-Fenton process under visible light. *Nanomaterials*, 43(21),

- 3341–3354. <https://doi.org/10.1080/09593330.2021.1921052>
6. Cycon M., Mroziak A., Piotrowska-Seget Z. 2019. Antibiotics in the soil environment—degradation and their impact on microbial activity and diversity. *Frontier in Microbiology*, 10(338), 1–45. <https://doi.org/10.3389/fmicb.2019.00338>
  7. Ersan M., Dogan H. 2023. Investigation of environmentally friendly adsorbent synthesis from eggshell by carbonization, immobilization, and radiation: Box-Benken Design and tetracycline removal. *Groundwater for Sustainable Development*, 20, 1–11. <https://doi.org/10.1016/j.gsd.2022.100858>
  8. Fatimah I., Wijayana A., Ramanda G.D., Suratno., Sagadevan S., Oh W., Doong R. 2024. Highly active photocatalyst of nickel oxide nanoparticles green-synthesized using *Tinospora cordifolia*-plant extract for photocatalytic oxidation of tetracycline. *Environmental Nanotechnology. Monitoring & Management*, 22, 1–10. <https://doi.org/10.1016/j.enmm.2024.100968>
  9. Fu Q., Meng Y., Yao Y., Shen H., Xie B., Ni Z., Xia S. 2023. Construction of facet orientation-supported Z-scheme heterojunction of BiVO<sub>4</sub> (110)-Fe<sub>2</sub>O<sub>3</sub> and its photocatalytic degradation of tetracycline. *Journal of Environmental Chemical Engineering*, 11(5), 1–12. <https://doi.org/10.1016/j.jece.2023.111060>
  10. Gogoi D., Das M.R., Ghosh N.N. 2023. 2-D gC<sub>3</sub>N<sub>4</sub> supported CoFe<sub>2</sub>O<sub>4</sub> nanoparticles as an efficient S-scheme catalyst for various antibiotic degradation. *Applied Surface Science*, 619, 1–11. <https://doi.org/10.1016/j.apsusc.2023.156753>
  11. Golrizkhatami F., Taghavi L., Nasseh N., Panahi H.A. 2023. Synthesis of novel MnFe<sub>2</sub>O<sub>4</sub>/BiOI green nanocomposite and its application to photocatalytic degradation of tetracycline hydrochloride: (LC-MS analyses, mechanism, reusability, kinetic, radical agents, mineralization, process capability, and purification of actual pharmaceutical wastewater). *Journal of Photochemistry & Photobiology, A: Chemistry*, 444, 1–16. <https://doi.org/10.1016/j.jphotochem.2023.114989>
  12. Guan H., Chen Y., Xue Y. 2024. A novel Fe<sub>3</sub>O<sub>4</sub>@Pt synthesized via a self-assembly strategy as efficient Fenton-like@mimetic enzyme catalyst for degradation of tetracyclines in food processing wastewater. *Colloids and Surfaces A: Physicochemical and Engineering Aspects*, 695, 1–12. <https://doi.org/10.1016/j.colsurfa.2024.134260>
  13. Guo J., Huang M., Gao P., Zhang Y., Chen H., Zheng S., Mu T., Luo X. 2020. Simultaneous robust removal of tetracycline and tetracycline resistance genes by a novel UiO/TPU/PSF forward osmosis membrane. *Chemical Engineering Journal*, 398, 1–11. <https://doi.org/10.1016/j.cej.2020.125604>
  14. Habiba U., Lee J.J.L., Joo T.C., Ang B.C., Afifi A.M. 2019. Degradation of Methyl orange and Congo red by using chitosan/polyvinyl alcohol/TiO<sub>2</sub> electrospun nanofibrous membrane. *International Journal of Biological Macromolecules*, 131, 821–827. <https://doi.org/10.1016/j.ijbiomac.2019.03.132>
  15. Han W., Shou J., Zhu S., Tu X., Chen Y., Sun C., Chang Y., Zheng H. 2024. Efficient electron transport between NiO/Fe<sub>2</sub>O<sub>3</sub> by loading amorphous carbon improves photocatalytic degradation property. *Journal of Environmental Chemical Engineering*, 12(1), 1–12. <https://doi.org/10.1016/j.jece.2023.111667>
  16. Hariani P.L., Salni S., Said M., Farahdiba R. 2022. Core-shell Fe<sub>3</sub>O<sub>4</sub>/SiO<sub>2</sub>/TiO<sub>2</sub> magnetic modified Ag for the photocatalytic degradation of Congo red dye and antibacterial activity. *Bulletin of Chemical Reaction Engineering & Catalysis*, 18(2), 315–330. <https://doi.org/10.9767/bcrec.19275>
  17. Hariani P.L., Said M., Salni, Rachmat A., Aprinati N., Stephanie, E.A. 2023. Synthesis of Fe<sub>3</sub>O<sub>4</sub>/SiO<sub>2</sub>/NiO magnetic composite: Evaluation of its catalytic activity for methylene blue degradation. *Global NEST Journal*, 25(2), 36–43. <https://doi.org/10.30955/gnj.004407>
  18. Harikumar B., Subhiksha V., Okla M.K., Abdelmaksoud M.A., El-Tayed M.A., Alatar A.A., Al-Amri S.S., Elbadawi Y.B., Sivaranjani P.R., Khan S.S. 2024. Magnetic Fe<sub>3</sub>O<sub>4</sub> nanospheres supported N/S-SnO<sub>2</sub> nanorod for highly effective visible light photocatalytic degradation of tetracycline. *Journal of Alloys and Compounds*, 986, 1–9. <https://doi.org/10.1016/j.jallcom.2024.174017>
  19. Huang K., Xu W., Zheng S., Tian J. 2023. Coupling photothermal and piezoelectric effect in Bi<sub>4</sub>Ti<sub>3</sub>O<sub>12</sub> for enhanced photodegradation of tetracycline hydrochloride. *Optical Materials*, 145, 1–12. <https://doi.org/10.1016/j.optmat.2023.114352>
  20. Islam M.A., Nazal M.K., Akinpelu A.A., Sajid M., Alhussain N.A., Billah R.E.K., Bahsis L. 2024. Novel activated carbon derived from a sustainable and low-cost palm leaves biomass waste for tetracycline removal: Adsorbent preparation, adsorption mechanisms and real application. *Diamond and Related Materials*, 147, 1–12. <https://doi.org/10.1016/j.diamond.2024.111375>
  21. Jayaprakash R.N., Dineshababu N., Selvaraj S., Vignesh S., Arun T., Ravichandran K. 2024. Hydrothermally constructed and visible-light activated efficient NiO/ZnO/g-C<sub>3</sub>N<sub>4</sub> ternary nanocomposites for Methylene blue dye degradation and antibacterial applications. *Inorganic Chemistry Communications*, 159, 1–12. <https://doi.org/10.1016/j.inoche.2023.111643>
  22. Jiang H., Wang Q., Chen P., Zheng H., Shi J., Shu H., Liu Y. 2022. Photocatalytic degradation of tetracycline by using a regenerable (Bi)BiOBr/rGO composite. *Journal of Cleaner Production*, 339, 1–10.

- <https://doi.org/10.1016/j.jclepro.2022.130771>
23. Kamoun E.A., Kenawy E.S., Chen X. 2017. A review on polymeric hydrogel membranes for wound dressing applications: PVA-based hydrogel dressings. *Journal of Advanced Research*, 3, 217–233. <https://doi.org/10.1016/j.jare.2017.01.005>
  24. Kouotou P.M., Kasmi A.E., Wu L., Waqas M., Tian Z. 2018. Kouotou Particle size-band gap energy-catalytic properties relationship of SE-CVD-derived Fe<sub>3</sub>O<sub>4</sub> thin films. *Journal of the Taiwan Institute of Chemical Engineers*, 93, 427–435. <https://doi.org/10.1016/j.jtice.2018.08.014>
  25. Li C., Zhang X., Wen S., Xiang R., Han R., Tang W., Yue T., Li Z. 2020. Interface engineering of zeolite imidazolate framework-8 on two-dimensional Al-metal-organic framework nanoplates enhancing performance for simultaneous capture and sensing tetracyclines. *Journal of Hazardous Materials*, 395, 1–10. <https://doi.org/10.1016/j.jhazmat.2020.122615>
  26. Li L., Han X., Feng S., Sun Z., Wang C. 2024. Ingenious design of II-scheme heterojunction BiVO<sub>4</sub>/COF for synergistic photocatalytic degradation of tetracycline. *Journal of Solid State Chemistry*, 338, 1–10. <https://doi.org/10.1016/j.jssc.2024.124888>
  27. Liu D., Lu L., Wang M., Hussain B., Tian S., Luo W., Zhou J., Yang Z. 2019. Tetracycline uptake by pak choi grown on contaminated soils and its toxicity in human liver cell line HL-7702. *Environmental Pollution*, 253, 312–321. <https://doi.org/10.1016/j.envpol.2019.06.086>
  28. Long Z., Xian G., Zhang G., Zhang T., Li X. 2020. BiOCl-Bi<sub>12</sub>O<sub>17</sub>Cl<sub>2</sub> nanocomposite with high visible-light photocatalytic activity prepared by an ultrasonic hydrothermal method for removing dye and pharmaceutical. *Chinese Journal of Catalysis*, 41(3), 464–473. [https://doi.org/10.1016/S1872-2067\(19\)63474-1](https://doi.org/10.1016/S1872-2067(19)63474-1)
  29. Luk C.J., Yip J., Yuen C.W.M., Kan C., Lam K. 2014. A Comprehensive study on adsorption behaviour of Direct, Reactive and Acid dyes on cross-linked and non-crosslinked chitosan Beads. *Journal of Fiber Bioengineering & Informatics*, 7, 35–52. <https://doi.org/10.3993/jfbi03201404>
  30. Marzbali M.H., Esmaili M., Abolghasemi H., Marzbali M.H. 2016. Tetracycline adsorption by H<sub>3</sub>PO<sub>4</sub>-activated carbon produced from apricot nut shells: A batch study. *Process Safety and Environmental Protection*, 102, 700–709. <https://doi.org/10.1016/j.psep.2016.05.025>
  31. Mohammadkhani A., Mohammadkhani F., Farhadyar N., Sadjadi M.S., Kianfar E. 2024. Novel nanocomposite zinc phosphate/polyvinyl alcohol/carboxymethyl cellulose: Synthesis, characterization and investigation of antibacterial and anti-corrosive properties. Case Studies. *Chemical and Environmental Engineering*, 9, 1–12. <https://doi.org/10.1016/j.cscee.2023.100591>
  32. Qin D., Hu W., Li Z. 2024. Green synthesis of β-cyclodextrin conjugated Fe<sub>3</sub>O<sub>4</sub>/NiO nanocomposites and its synergistic effect of adsorption and photocatalytic degradation for Congo red removal. *Desalination and Water Treatment*, 317, 1–10. <https://doi.org/10.1016/j.dwt.2024.100136>
  33. Qin Y., Chai B., Wang C., Yan J., Fan G., Song G. 2022. Removal of tetracycline onto KOH-activated biochar derived from rape straw: Affecting factors, mechanisms and reusability inspection. *Colloids and Surfaces A. Physicochemical and Engineering Aspects*, 640, 1–11. <https://doi.org/10.1016/j.colsurfa.2022.128466>
  34. Said M., Rizki W.T., Asri W.R., Desnelli D., Rachmat A., Hariani PL. 2022. SnO<sub>2</sub>-Fe<sub>3</sub>O<sub>4</sub> nanocomposites for the photodegradation of the Congo red dye. *Heliyon*, 8, 1–8. <https://doi.org/10.1016/j.heliyon.2022.e09204>
  35. Saitoh T., Shibata K., Fujimori K., Ohtani Y. 2017. Rapid removal of tetracycline antibiotics from water by coagulation-flotation of sodium dodecyl sulfate and poly(allylamine hydrochloride) in the presence of Al(III) ions. *Separation and Purification Technology*, 187, 76–83. <https://doi.org/10.1016/j.seppur.2017.06.036>
  36. Sanchez-Machoda D.I., Lopez-Cervantes J., Vega-Cazarez C.A., Hernandez-Ruiz K.L., Campas-Baypoli O.N., Soto-Cota A., Madera-Santana T.J. 2024. Functional and antibacterial characterization of electrospun nanofiber membranes made of chitosan and polyvinyl alcohol. *Results in Chemistry*, 7, 1–13. <https://doi.org/10.1016/j.rechem.2024.101314>
  37. Sharma M., Mandal M.K., Pandey S., Kumar R., Dubey K.K. 2022. Visible-light-driven photocatalytic degradation of tetracycline using heterostructured Cu<sub>2</sub>O-TiO<sub>2</sub> nanotubes, kinetics, and toxicity evaluation of degraded products on cell lines. *ACS Omega*, 7, 33572–33586. <https://doi.org/10.1021/acsomega.2c04576>
  38. Shaban M., Ahmed A.M., Shehata N., Betiha M.A., Rabie MA. 2020. Ni-doped and Ni/Cr co-doped TiO<sub>2</sub> nanotubes for enhancement of photocatalytic degradation of Methylene blue. *Journal of Colloid and Interface Science*, 555, 31–41. <https://doi.org/10.1016/j.jcis.2019.07.070>
  39. Siddhardhan E.V, Surender S., Arumanayagam T. 2023. Degradation of tetracycline drug in aquatic environment by visible light active CuS/CdS photocatalyst. *Inorganic Chemistry Communications*, 147, 1–10. <https://doi.org/10.1016/j.inoche.2022.110244>
  40. Sopanrao K.S., Sreedhar I. 2024. Polyvinyl alcohol modified chitosan composite as a novel and efficient adsorbent for multi-metal removal. *Separation*

- and Purification Technology*, 340, 1–18. <https://doi.org/10.1016/j.seppur.2024.126731>
41. Tripta., Rana P.S. 2023. Structural, optical, electrical, and photocatalytic application of NiFe<sub>2</sub>O<sub>4</sub>@NiO nanocomposites for Methylene blue dye. *Ceramics International*, 49(9), 13520–13530. <https://doi.org/10.1016/j.ceramint.2022.12.227>
  42. Tumbelaka R.M., Istiqomah N.I., Kato T., Oshima D., Suharyadi E. 2022. High reusability of green-synthesized Fe<sub>3</sub>O<sub>4</sub>/TiO<sub>2</sub> photocatalyst nanoparticles for efficient degradation of methylene blue dye. *Materials Today Communications*, 33, 1–15. <https://doi.org/10.1016/j.mtcomm.2022.104450>
  43. Vijeth H., Ashokkumar S.P., Yesappa L., Vandana M., Devendrappa H. 2020. Hybrid core-shell nanostructure made of chitosan incorporated polypyrrole nanotubes decorated with NiO for all-solid-state symmetric supercapacitor application. *Electrochimica Acta*, 354, 1–14. <https://doi.org/10.1016/j.electacta.2020.136651>
  44. Vishwakarma A.K., Yadav B.S., Singh A.K., Kumar S., Kumar N. 2023. Magnetically recyclable ZnO coated Fe<sub>3</sub>O<sub>4</sub> nanocomposite for MO dye degradation under UV-light irradiation. *Solid State Sciences*, 145, 1–11. <https://doi.org/10.1016/j.solidstatesciences.2023.107312>
  45. Wang J., Chu L., Wojnarovits L., Takacs E. 2020. Occurrence and fate of antibiotics, antibiotic resistant genes (ARGs) and antibiotic resistant bacteria (ARB) in municipal wastewater treatment plant: An overview. *Science of The Total Environment*, 744, 1–12. <https://doi.org/10.1016/j.scitotenv.2020.140997>
  46. Wei X., Naraginti S., Chen P., Li J., Yang X., Li B. 2023. Visible light-driven photocatalytic degradation of tetracycline using p-n heterostructured Cr<sub>2</sub>O<sub>3</sub>/ZrO<sub>2</sub> nanocomposite. *Water*, 15(3702), 1–15. <https://doi.org/10.3390/w15203702>
  47. Yan R., Wang Y., Li J., Wang X., Wang Y. 2022. Determination of the lower limits of antibiotic biodegradation and the fate of antibiotic resistant genes in activated sludge: Both nitrifying bacteria and heterotrophic bacteria matter. *Journal of Hazardous Materials*, 425, 1–12. <https://doi.org/10.1016/j.jhazmat.2021.127764>
  48. Yuan X., Yang J., Yao Y., Shen H., Meng Y., Xie B., Ni Z., Xia S. 2022. Preparation, characterization and photodegradation mechanism of 0D/2D Cu<sub>2</sub>O/BiOCl S-scheme heterojunction for efficient photodegradation of tetracycline. *Separation and Purification Technology*, 291, 1–11. <https://doi.org/10.1016/j.seppur.2022.120965>
  49. Zhao R., Sun X., Jin Y., Han J., Wang L., Liu F. 2019. Au/Pd/g-C<sub>3</sub>N<sub>4</sub> nanocomposites for photocatalytic degradation of tetracycline hydrochloride. *Journal of Materials Science*, 54, 5445–5456. <https://doi.org/10.1007/s10853-018-03278-7>
  50. Zhao C., Ma J., Li Z., Xia H., Liu H., Yang Y. 2020. Highly enhanced adsorption performance of tetracycline antibiotics on KOH-activated biochar derived from reed plants. *RSC Advances*, 10, 5066–5076. <https://doi.org/10.1039/C9RA09208K>
  51. Zhang Y., Liu F., Zhong L., Dong Z., Chen C., Xu Z. 2023. Reusable and environmentally friendly cellulose nanofiber/titanium dioxide/chitosan aerogel photocatalyst for efficient degradation of tetracycline. *Applied Surface Science*, 641, 1–13. <https://doi.org/10.1016/j.apsusc.2023.158425>
  52. Zhu L., Zhou Y., Fei L., Cheng X., Zhu X., Deng L., Ma X. 2022. Z-scheme CuO/Fe<sub>3</sub>O<sub>4</sub>/GO heterojunction photocatalyst: Enhanced photocatalytic performance for elimination of tetracycline. *Chemosphere*, 309(2), 1–10. <https://doi.org/10.1016/j.chemosphere.2022.136721>